RESEARCH ARTICLE

Dehydration-driven mass loss from packs of sintering hydrous silicate glass particles

Jérémie Vasseur[1] 🔵 | **Fabian B. Wadsworth[2]** | **Yan Lavallée[1]** | **Donald B. Dingwell[1]**

[1]Earth & Environmental Sciences, Ludwig-Maximilians-Universität, Munich, Germany

[2]Earth Sciences, Durham University, Science Labs, Durham, UK

Correspondence

Jérémie Vasseur, Earth & Environmental Sciences, Ludwig-Maximilians-Universität, Theresienstr. 41, 80333 Munich, Germany.
Email: j.vasseur@lmu.de

Funding information

European Research Council, Grant/Award Numbers: 834225, 101001065; Natural Environment Research Council, Grant/Award Number: NE/T007796/1

Abstract

Glass sintering involves the densification of packs of particles and the expulsion of the interparticle pore gas. The pore space begins as a convolute interconnected interparticle network, and ends as distributed isolated bubbles; two configurations that are separated by the percolation threshold. Here, we perform experiments in which (i) the particles are initially saturated in H_2O at 871 K, and (ii) they are then heated non-isothermally at different rates to temperatures in excess of 871 K. In step (ii), H_2O becomes supersaturated and the particles diffusively lose mass as they sinter together. We use thermogravimetry to track the loss of mass with time. We find that the mass loss is initially well predicted by solutions to Fick's second law in spherical coordinates with the appropriate material and boundary conditions. However, as the sintering pack crosses the percolation threshold at a time predicted by sintering theory, we find that the mass loss deviates from simple diffusional solutions. We interpret this to be the result of an increase in the diffusion distance from the particle-scale to the scale of the sintering pack itself. Therefore, we conclude that the open- to closed-system transition that occurs at the percolation threshold is a continuous, but rapid jump for diffusive and other transport properties. We use a capillary Peclet number Pc to parameterize for this transition, such that at low Pc diffusive equilibrium is achieved before the sintering-induced transition to closed system, whereas at high Pc there is a "diffusion crisis" and disequilibrium may be maintained for longer relative timescales that depend on the system size.

KEYWORDS

diffusion/diffusivity, glass transition, hydration, sinter/sintering, soda-lime-silica

1 | INTRODUCTION

Sintering of viscous particles (or droplets)—such as silicate glass particles softened at high temperature—is relevant to a wide range of ceramic,[1–3] glass,[4,5] metal,[6] and polymer[7] manufacture processes, to our understanding of volcanic welding and spatter agglutination,[8–13] and to the potential for sintering production of building materials on other planets.[14] These processes ubiquitously involve the creeping flow of fluid at the contact points between droplets such that the internal surface area of a many-droplet system is minimized.[15] This typically occurs in the regime

where fluid motion is driven by interfacial stress $P \approx 2\Gamma/R$, where Γ is the interfacial tension between the droplet fluid and the interstitial pore fluid and R is a characteristic droplet radius.[15–18] The interfacial (or capillary) regime is characterized by a high Ohnesorge number $Oh = \mu/\sqrt{\rho\Gamma R}$ and a small Eötvös number $Eo = \rho g R^2/\Gamma$, such that inertial and body forces from gravity are negligible. (Here ρ is the droplet density, μ is the droplet viscosity, and g is the acceleration due to gravity.) Sintering in this regime has received detailed attention resulting in models for the evolution of surface area in systems of a few droplets[19] or of the inter-droplet pore volume fraction ϕ in systems of many droplets.[13,15,16] In the latter case, extensions of simple models have been made for arbitrary droplet size distribution[1,18] or for situations in which the droplet viscosity is an arbitrary function of time.[15] In much of this work, it is implicit that sintering ends with a regime transition from an open-system interparticle network, to an isolated and closed system of bubbles in a melt, with an associated drop in permeability to zero.[12,20,21] The implications of this regime transition are crucial when other transport properties in the gas phase are important, and yet these implications have not received much attention.

Sintering in reactive atmospheres—including humid atmospheres with high relative H_2O partial pressures—is commonplace in the Earth system[22,23] and may be advantageous for industrial processes.[24] However, sintering in the presence of any reactive gas species presents challenges. Among those challenges is the possibility that the gas may diffuse into or out of the particles during sintering, which can change the physical properties of the particles (and the viscosity in particular), and therefore affect sintering rates in a hysteretic feedback loop.[11] To take H_2O as an example, even small amounts of diffusive mass movement of volatile H_2O species into or out of silicate particles can result in large changes in liquid viscosity[25,26] and can induce spatial gradients of viscosity at droplet surfaces. Such diffusion into or out of the particles could also induce or inhibit crystallization.[27] Therefore, the possibility that gas species may diffuse during sintering requires specific research attention. Here, our contribution focuses on two aspects of this problem: (i) first, how does diffusion of H_2O out of particles affect the overall sintering rate via the associated known increase in viscosity; and (ii) what is the ultimate effect of the percolation threshold on the diffusion process as a sintering system moves from open to closed? The latter question is motivated by the intuition that free exchange of gas into or out of the particles is determined by the thermodynamic "openness" of the pore space and the connectivity with the exterior atmosphere. We perform and analyze new experiments specifically designed to address these questions.

2 | THEORETICAL BACKGROUND

Here, we introduce a theoretical basis for the two principal processes investigated here: (a) sintering of high-temperature glass particles; and (b) diffusive mass transport of H_2O into or out of particles. While there are various theoretical approaches to both of these problems, we do not attempt a review or a model inter-comparison here, and instead we select model approaches that have been specifically used successfully for modeling sintering with diffusive mass transport occurring concomitantly.

2.1 | A model for sintering of silicate glass particles

The sintering of packed viscous droplets has received wide theoretical and experimental attention.[15–17,28] On the basis of high-resolution data across a wide range of temperatures, Wadsworth et al. (2016)[15] conclude that an adapted form of a *vented bubble model*[16] provides an excellent description of the kinetics of porosity ϕ changes for packed populations of initially spherical silicate droplets as a function of a characteristic pore radius a (previously shown to scale with the aforementioned characteristic droplet radius[18]), the liquid–vapor interfacial tension Γ, and the liquid viscosity μ as follows:

$$\frac{d\phi}{dt} = -\frac{3\Gamma}{2\mu a_i}\left(\frac{\phi_i}{1-\phi_i}\right)^{1/3}\phi^{2/3}(1-\phi)^{1/3} \quad (1)$$

where a_i and ϕ_i are the initial pore radius and porosity, respectively. This model is readily non-dimensionalized knowing that the characteristic time associated with coalescence of droplets driven by interfacial tension is the capillary timescale $\lambda_b = \mu a_i/\Gamma$, and that the porosity can be normalized by the initial porosity ϕ_i, we have

$$\frac{d\bar{\phi}}{d\bar{t}_b} = -\frac{3}{2}\left(\frac{1-\bar{\phi}\phi_i}{1-\phi_i}\right)^{1/3}\bar{\phi}^{2/3} \quad (2)$$

where $\bar{t}_b = t/\lambda_b$ is the dimensionless time for this process, and $\bar{\phi} = \phi/\phi_i$. When solving Equations (1) or (2), we use the method proposed by Wadsworth et al. (2017)[18] for finding a_i from the radius distribution of the sintering particles; this model is utilized herein.

2.2 | Diffusion of H_2O into or out of silicate particles

H_2O readily diffuses in silicate liquids as bubbles form or grow,[29] surfaces are created,[30] or as anhydrous crystals

nucleate and grow.[31] In each of these cases, the diffusion of H_2O can be modeled using Fick's second law, which in its general form relates the evolution of concentration C to the Laplacian spatial gradients of concentration ∇C and the diffusion coefficient D for that diffusing species $\partial C / \partial t = \nabla(D\nabla C)$, and when cast in one-dimensional (1D) spherical coordinates is[32]

$$\frac{\partial C}{\partial t} = \frac{1}{r^2} \frac{\partial}{\partial r} \left(r^2 D \frac{\partial C}{\partial r} \right) \qquad (3)$$

where t is the time after the onset of diffusion, r is the radial distance from the center of the sphere of radius R, and D is the diffusivity coefficient for the species C. Once D is known, Equation (3) can be solved to give the evolution of C in the sphere through time. Herein, we are concerned with the case when C is a total H_2O concentration (in wt%).

In detail, the speciation of water evolves to equilibrate hydroxyl OH^- groups with H_2O molecules in the silicate liquid structure.[33,34] However, here we take a simple total H_2O diffusivity D to represent the bulk mass transfer coefficient of total H_2O in spheres. We can use a general empirical exponential for temperature-dependent diffusivity laws that has been validated against experimental datasets and is[35]

$$D = \exp \left(d_0 - \frac{d_1}{T} \right) \qquad (4)$$

where d_0 and d_1 are empirical constants to be determined (discussed later). When looking for solutions to Equation (3), we must define initial and boundary conditions. Because we aim to perform two types of experiment (described later), these will change. But in both cases, we will need to know the solubility of H_2O, C_e, as a function of the experimental temperature. A convenient functional form is[36,37]

$$C_e = \exp \left(c_0 + \frac{c_1}{T - c_2} \right) \qquad (5)$$

where c_0, c_1, and c_2 are constants to be determined (discussed later). We non-dimensionalize Equations (3) and (4) by making the following substitutions:

$$\bar{C} = \frac{C}{C_e}; \bar{t}_d = \frac{t}{\lambda_d} = \frac{D_i}{R^2} t; \bar{D} = \frac{D}{D_i}; \bar{d}_1 = \frac{d_1}{T_i} \qquad (6)$$

where a subscript i denotes an initial value, a subscript e denotes the equilibrium value, and a bar above a parameter represents its dimensionless form. We note that the dimensionless time is found by normalizing the experimental time by the characteristic diffusion time λ_d. Here, $D_i = \exp(d_0 - d_1/T_i)$. This gives us a non-dimensional

form of Equations (3) and (4) as follows:

$$\frac{\partial \bar{C}}{\partial \bar{t}_d} = \frac{1}{\bar{r}^2} \frac{\partial}{\partial \bar{r}} \left(\bar{r}^2 \bar{D} \frac{\partial \bar{C}}{\partial \bar{r}} \right)$$

$$\bar{D} = \exp \left[\bar{d}_1 \left(1 - \frac{1}{\bar{T}} \right) \right] \qquad (7)$$

Equation (7) can then be solved numerically using a backward-time centered-space implicit finite difference scheme with a relaxed fixed-point method to ensure convergence at each step. We use this model to assess the temporal and spatial evolution of H_2O for a given initial condition and a set of boundary conditions.

2.3 | Non-isothermal conditions

We can account for non-isothermal conditions by integrating the temperature-dependent parameters in both the sintering and the diffusion problems dealt with here. For sintering, both Γ and a_i are constants, and so μ is the temperature-dependent parameter. While Γ and a_i can be affected by temperature,[38] this is negligible[15] compared with the effect of temperature on μ (note that the pore radius a, rather than the initial value a_i, is a function of time in the model; Equation 1). Therefore, the dimensionless sintering time is found by

$$\bar{t}_b = \frac{\Gamma}{a_i} \int_0^t \frac{1}{\mu} dt \qquad (8)$$

where $\bar{t}_b$ allows extension to non-isothermal conditions. Similarly, the diffusion times can be integrated in non-isothermal conditions to give a universal $\bar{t}_d$ that does not depend on the thermal path taken. As with $\bar{t}_b$ (Equation 8), this is found by noting that R is a constant (neglecting very minor thermal expansivity effects), and so D is the time-dependent parameter as temperature changes, yielding:

$$\bar{t}_d = \frac{1}{R^2} \int_0^t D dt \qquad (9)$$

where $\bar{t}_d$ extends the diffusion problem to non-isothermal conditions.

2.4 | Polydisperse solutions

As a final theoretical step, we acknowledge herein that the sintering particles that are subject to mass diffusion are polydisperse. To account for this, we convolve the sintering law (e.g., Equation 2) with the pore size distribution (found from the particle size distribution via

Wadsworth et al., 2017[18]) to arrive at the convolved average $\bar{t}_b$, which has been shown to accurately account for polydisperse sintering.[18] In an identical manner, we convolve the diffusion law (e.g., Equation 7) with the particle size distribution to find a volume-averaged diffusion time $\bar{t}_d$, shown to accurately predict diffusive mass transport in particles that are polydisperse in size.[39]

3 | EXPERIMENTAL MATERIAL AND METHODS

3.1 | Material selection and characterization

For our experimental campaign, we use spherical Spheriglass soda-lime-silica glass beads from Potters Industries as an experimental sintering material. We chose a population of beads with a monodisperse size distribution about a mean radius of $\langle R \rangle = 188 \pm 41\ \mu$m (the uncertainty is given by 1σ on the measured distribution). These beads have a reproducible heat-capacity evolution through the glass transition interval, do not show liquid–liquid immiscibility, and do not crystallize on the timescale of the experimental campaign presented here.[8,15]

As a first step, we aim to constrain the material properties of the glass beads used herein. The diffusivity of H_2O, D; the solubility concentration of H_2O, C_e; and the viscosity, μ, for this glass are well known,[18,35] whereas no description of the concentration dependence of the diffusivity of H_2O[35] is available. Using data for $D(T)$ compiled for soda-lime-silica glasses (and compositionally similar float glass) and liquids,[35–37,40] we fit Equation (4) to published data in the range 600–1800 K, we find that $d_0 = -9.84 \pm 0.33$ and $d_1 = 18\,692.52 \pm 342.20$ K (Figure 1A). We follow Shelby (2008)[35] in fitting Equation (5) to a published dataset for glass of the same composition,[37,36] whence we obtain the empirical constants $c_0 = -2.25 \pm 0.02$, $c_1 = 29.56 \pm 12.42$ K and $c_2 = 777.40 \pm 30.85$ K (Figure 1B). Finally, we use the model of Deubener et al. (2008)[41] for the viscosity law $\mu(T, C)$ (Figure 1C), comprising the temperature-dependent parameters used below.

3.2 | Creating hydrous glass beads and electron microprobe determinations

We poured ~10g of beads into a high-temperature gas-particle reactor[42] and heated them to 871 K (above their glass transition temperature), tumbling them gently to avoid sintering, sticking, and coalescence. At this temperature, $C_e = 0.144$ wt% (Equation 5; Figure 1B). We continuously flushed the reactor atmosphere with a mixture
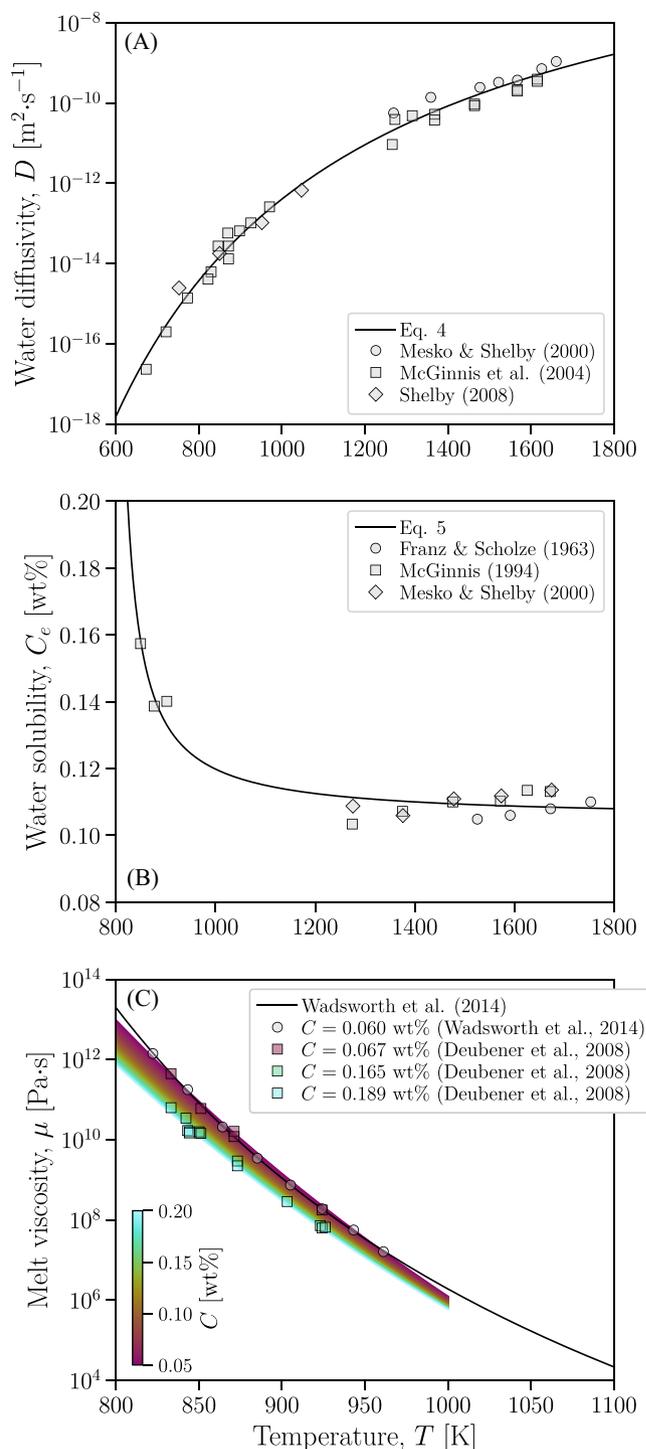
FIGURE 1 The physical properties of the soda-lime-silica glass used herein, constrained using literature data. (A) Diffusivity of H_2O,D, as a function of temperature; data are fit to Equation (4) (see text for parameter values). (B) The solubility of H_2O,C_e, as a function of temperature; data are fit to Equation (5) (see text for parameter values). (C) The viscosity,μ, as a function of temperature and dissolved H_2O concentration; data are fit according to Deubener et al. (2008).[41] Also shown is the anhydrous non-Arrhenian form $\mu = \exp(m_0 + m_1/(T - m_2))$ with $m_0 = -15.62$, $m_1 = 17\,227.29$ K, and $m_2 = 427.33$ K presented in Wadsworth et al. (2014)[8]

of 5 wt% nebulized water droplets and 95 wt% high-purity (5.0, 99.9%) argon. The water droplets quickly flashed to steam and increased the humidity of the furnace atmosphere. After 16.5 h of continuous exposure, we stopped the flow of water and cooled the furnace rapidly. The glass bead diameters are sufficiently low to preclude direct determination of H_2O profiles in the post-hydration samples by conventional techniques (e.g., Fourier transform infrared spectroscopy), which is discussed later.

To ensure no leaching of the glass occurred during hydration experiments and that the composition remained unaffected, we measured the local chemical composition of the glass beads using polished thick sections of sintered and unsintered samples before and after hydration. We did this using a Cameca SX100 electron microprobe using a 15 kV accelerating voltage at a current of 5 nA and a defocused beam size of 10 μm. We calibrated the wavelength dispersive spectrometers using crystal standards.

3.3 | Sintering and mass loss determination

The experiment described in Section 3.2 resulted in partially hydrated glass beads exhibiting diffusive gradients of increasing H_2O content from their interiors to their surfaces. In a second step, we aimed to sinter packs of these beads in an anhydrous atmosphere such that the initial externally imposed chemical gradient is reversed, and dehydration through diffusive transport of H_2O to the surface occurs. We might anticipate that beads in this second experiment would dehydrate back toward their initial (approximately) anhydrous state. Thus, after exposure to the hydrous atmosphere in the reactor, ~60 mg of glass beads were transferred to a Netzsch Pegasus 404 simultaneous thermal analyzer in an open-topped platinum crucible, lightly packed together, and heated to 1350 K at linear non-isothermal temperature rates in three experiment types. The three experiments were performed at 2, 5, and 10 K min^{-1}, respectively. This heating was performed in a nominally dry pure argon (5.0 purity) atmosphere. The time-dependent sample mass was measured relative to an empty reference platinum crucible. Multiple heating and cooling cycles were performed to ensure that the first heating ramp indeed resulted in a maximum mass loss. In this experiment, continuous mass data were collected and converted to time-dependent $C(t)$ by assuming that all sample mass loss is water loss. At the end of the experiments, visual inspection confirmed that sintering had occurred, such that the end-product was a dense glass in the crucible with a homogeneous appearance, that is no longer composed of loose glass beads, with a small number of isolated spherical bubbles in the glass, visible by binocu-

lar microscope. The final porosity ϕ_f was determined by helium pycnometry using an Ultrapyc 1200e from Quantachrome. This device allows us to determine the density of the sintered mass ρ_b, which can be used to compute the porosity via $\phi_f = 1 - \rho_b/\rho$, and $\rho = 2500$ kg m^{-3} is the glass density given by the manufacturer.

4 | RESULTS AND ANALYSIS

Our methodology involves two steps: (i) a hydration experiment in which glass beads are partially hydrated in a H_2O-rich atmosphere at high temperature, and (ii) a dehydration experiment in which the mass of a pack of sintering glass beads is recorded with time. Here, we report the results of these experiments, as well as our analysis in which we compare our results with the theoretical predictions made using Section 2. Because the hydration H_2O profiles are analytically un-measurable at the lengthscales of the glass beads (see Section 3), we treat the *forward model* of the hydration followed by dehydration (see Section 3.2) as a robust test of both the mass loss and the hydration step. If our hydration model for the hydration temperature and time were inaccurate, then this inaccuracy would propagate to our mass loss model, and the model would not match the data. Therefore, any match between our theoretical calculation and the measurements represents a robust test in aggregate.

4.1 | Experimental hydration of glass beads

We take the measured experimental temperature ($T = 871$ K) along with the material properties determined in Section 3.1 (Figure 1), in order to predict the profile of H_2O that would be expected after the experimental time ($t = 5.94 \times 10^4$ s). We assume that $C = 0$ wt% at all r for $t = 0$ s, and that $dC/dr = 0$ and $C = C_e$ (calculated from Equation 5) at $r = 0$ and $r = R$, respectively. Using these initial and boundary conditions with Equation (7), we find the $C(r)$ curve shown in Figure 2. This curve results from a progressive hydration of the beads with an inward-propagating front of H_2O. Electron microprobe analyses confirmed that other than H_2O, the glass samples remained chemically homogeneous and that no leaching occurred during hydration.

4.2 | Bulk mass loss during sintering

In the sintering experiment, we use a "dry" (5.0 purity) argon) atmosphere, which means that the partial pressure
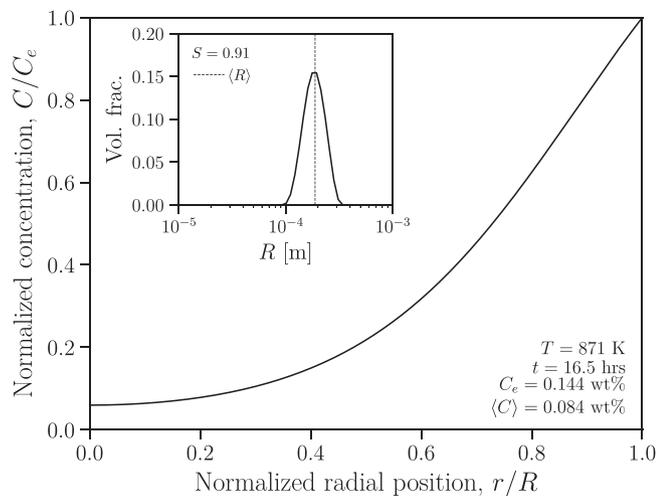
FIGURE 2 Normalized concentration gradient in the post-experiment glass particles, determined with a 1D diffusion model. Shown is the result of solving Equation (7) with relevant initial and boundary conditions, and the 16.5-h experimental isochron. *Inset*: the measured particle size distribution used herein (see discussion of polydisperse effects).

of H_2O is vanishingly low, and as such we anticipate that $C_e \approx 0.01$ wt%, a value typical of dehydration of particles at dry furnace conditions.[11,12,43] The result is that we expect the H_2O that had diffused into the beads in the first experiment (see Section 4.1) will essentially diffuse out of the beads in this second experiment. Because the spatial distribution of H_2O was not uniform after the hydration experiment (Figure 2), the dehydration will create complex diffusion profiles, as the H_2O equilibrates, and ultimately exits the glass beads altogether during dehydration. We can predict quantitatively what the evolution of H_2O distributions in the glass beads will look like as they are reheated in the sintering experiment. To do this, we solve Equation (7) but with new initial and boundary conditions. For this, we assume that initially $C = f(r)$ at all r, where $f(r)$ is the output spatial distribution after the hydration experiments (shown in Figure 2). Then we also assume that $dC/dr = 0$ and that $C = 0$ at $r = 0$ and $r = R$, respectively. In Figure 3, we show the forward model results predicting the evolution of the spatial distribution of H_2O as the hydrated glass beads are heated at the three heating rates used in the sintering experiments.

Our sintering experiments yield a bulk determination of the mass lost from the samples as they sinter (Figure 4). In order to compare the three experiments performed at different heating rates, we show the data as a function of temperature, where the transformation between time and temperature is via $T = T_i + qt$, where q is the heating rate used. In all cases, the mass of the samples decreases non-linearly but monotonically (Figure 4). The forward model for diffusive mass loss provides the local value of C, which
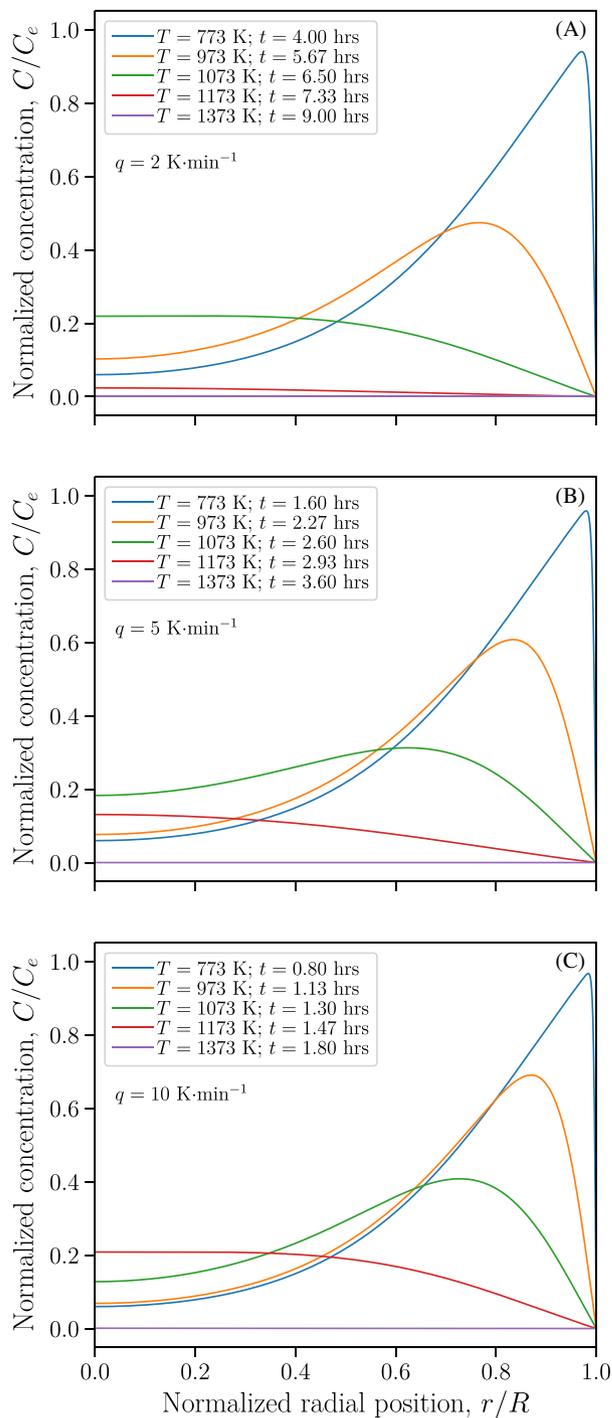
FIGURE 3 Forward modeling of the evolution of local H_2O concentration for our glass bead population during the sintering dehydration experiment after the initial hydration step for (A) 2 K min⁻¹, (B) 5 K min⁻¹, and (C) 10 K min⁻¹ constant heating rates. The initial profile of H_2O is taken to be the measured profile from Figure 2.

can be converted to a bulk average value $\langle C \rangle$ by solving the spherical volume integral[39]

$$\langle C \rangle = 3 \int_0^1 C \bar{r}^2 \, d\bar{r} \quad (10)$$
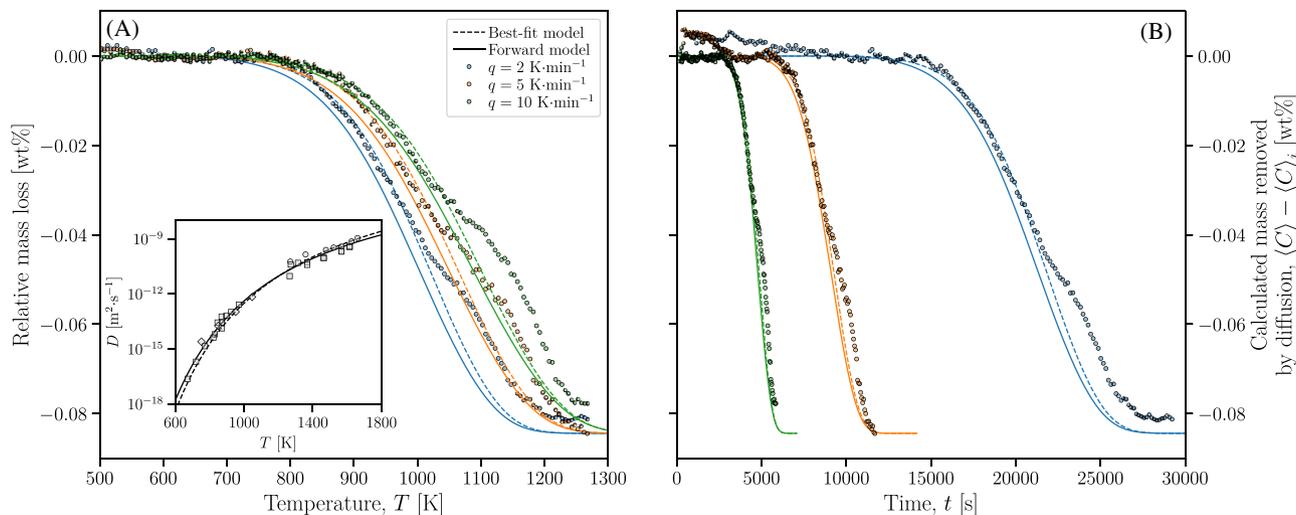
FIGURE 4 The measured change in bulk sample mass normalized to the initial mass for the three heating rates used herein. We also show the solution to the diffusion equation (Equation 7; Figure 3) cast as $\langle C \rangle - \langle C \rangle_i$ via Equation (10).

The mass lost from the bead is then $\langle C \rangle - \langle C \rangle_i$ for which $\langle C \rangle_i$ is $\langle C \rangle$ at $t = 0$ s. Using our diffusion model (Figure 3) and Equation (10), we can predict the mass loss at each time step, and therefore at each temperature step (Figure 4). Without fitting, this result shows a broad match to our data, albeit slightly lower than the observed mass at any given time or temperature. To improve the model prediction with respect to our data, we use the same model, but minimize for the $D(T)$ parameter inputs (i.e., d_0 and d_1; Equation 4) globally for all experiments. We find that this not only improves the match between our theory and the data (Figure 4) but also does not render our $D(T)$ curve prediction (from the minimization of d_0 and d_1) inconsistent with the previous experimental $D(T)$ outputs (Figure 4A *inset*).

Even with the improved fit of our data to the mass-loss predictions from theory, we note that the shape of the curve traced by the measured continuous data diverges at critical temperatures T' (different temperatures depending on the heating rate; Figure 4), above which the model predictions appear insufficient. We hypothesize that the deviation between the model and our data is associated with the fact that the glass beads are sintering as they lose mass.

4.3 | Syn-sintering mass diffusion

In Section 4.2, we noted that the spherical diffusion model provides an excellent description of the continuous mass loss data up to a critical temperature T', above which the data deviate from the model predictions. First, we transform the temperature T back to time t (see Figure 4B),
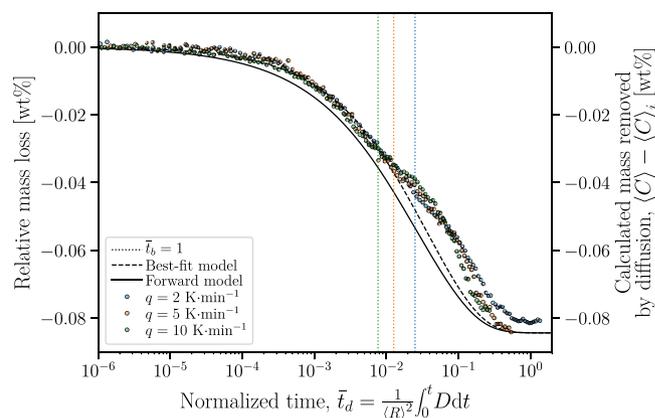
FIGURE 5 Relative mass loss versus normalized timescales. Application of our integral solution for non-isothermal diffusion (via Equations 9 with 7) demonstrates that all data and model solutions collapse to a universal description with dimensionless time $\bar{t}_d$. Also shown are the values of $\bar{t}_d$ (dotted lines) at which $\bar{t}_b = 1$ occurs (see text for details), representing the completion of sintering at each quench rate.

and then apply the normalization of time via Equation (9), which results in a collapse of the data to a single description (Figure 5), showing that the predicted time at which equilibrium is attained is $\bar{t}_d \sim 1$. In this normalized space, the data that deviated at different T', now deviate at three different values of $\bar{t}_d$.

In order to test if this deviation is associated with the sintering process, we solve Equation (2) for our system to find $\bar{\phi}(\bar{t}_b)$. This shows that the completion of sintering at $\bar{\phi} = 0$ occurs at $\bar{t}_b = 1$ (see previous work for confirmation of this[13]). Therefore, $\bar{t}_b = 1$ is a proxy for the transition to a completely sintered system. In order to compute the

value of $\bar{t}_d$ at which $\bar{t}_b = 1$, we must account for the effect of a gradient of H_2O concentration on the viscosity. The sintering model requires a single value of viscosity, and so, following the approach of Equation (10), we take the volume average viscosity $\langle \mu \rangle$. Hence, we adopt the following workflow: (i) compute the result of the diffusion equation (Equation 7) and output the volume average of H_2O concentration $\langle C \rangle$; (ii) use the law for viscosity as a function of H_2O concentration and temperature (see Figure 1C) to convert $\langle C \rangle$ into a modeled volume average viscosity $\langle \mu \rangle$ at a each time step; (iii) use Equation (8) to then compute the normalized time for the given temperature–time pathway (in this case imposed by a constant heating rate); (iv) find the time at which sintering completes, which is given by $\bar{t}_b = 1$; and finally (v) to use Equation (9) to find the equivalent time at which sintering completes in terms of the diffusion process.

In Figure 5, we show that the data collapse to a universal trend when normalized as the non-isothermal $\bar{t}_d$. This confirms that it is a diffusive loss process that is controlling the mass loss, even after the apparent "bump" in the data observed. In Figure 5, we also indicate the three values of $\bar{t}_d$ at which $\bar{t}_b$ would be equal to 1 as vertical dotted lines. Importantly, despite the fact that it is not minimized to the data in any manner, the positions of these transition points approximately coincide with the point beyond which the data deviate from the diffusion model (Figure 5) for all heating rates. This analysis demonstrates that the time beyond which the mass loss data deviate from our diffusion model coincides with the time at which sintering is predicted to be complete. Sintering involves the progressive isolation of pore space, and so it would be reasonable to assume that diffusive mass loss from particles that are also sintering would be impeded once sintering has progressed to an appreciable degree as seen here (Figure 5).

We experimentally confirm that the final end state of the process is indeed a completely sintered mass by determining the final porosity ϕ_f. We find that in the 2, 5, and 10 K min^{-1} experiments, ϕ_f was 0.041 ± 0.014, 0.036 ± 0.021, and 0.050 ± 0.021, respectively. These values are consistent with a wide range of measured final values in sintering experiments performed previously,[15–17,28] confirming empirically that sintering runs to completion in our experiments. In turn, this means that the sintered mass must have crossed the transition to isolated porosity.

5 | INTERPRETATION AND DISCUSSION

Our results show that hydration and dehydration of glass beads occur via radial diffusion into spheres, as might be expected. We validate the theory behind this diffusion process in a relatively complex situation in which hydration occurs at a single temperature and is terminated (via quenching) before hydration is complete and at equilibrium (note the profile remnant in the glass beads; Figure 2), and then re-heat the same samples that host a disequilibrium H_2O profile in a nominally dry environment at non-isothermal conditions in order to dehydrate them again. Despite this complexity, the theoretical approach taken here (e.g., Figure 3) provides a good match to the results for the bulk mass loss in the second experimental step (dehydration) up to a critical point, beyond which the data deviate from the description (Figure 4). The time at which that critical point occurs is consistent with the predicted time at which sintering is complete (Figure 5). The principal result thus far is the localization of the critical point and its interpretation in terms of the known dynamics that occur when particles sinter together. Next, we frame this discussion around parameterizing this apparent competition between mass transport processes by diffusion, and sintering processes by viscous flow.

The sintering timescale λ_b and the diffusion timescale λ_d can be used to frame a dimensionless group

$$\text{Pc} = \frac{\lambda_d}{\lambda_b} = \frac{R\Gamma}{\mu_i D_i} \qquad (11)$$

which has been referred to as a capillary Péclet number[11–13,44] and where μ_i and D_i are the initial values of those properties. If Pc $\gg 1$, then sintering will occur more rapidly than diffusion and so the concentration of H_2O in the glass beads will remain close to the initial disequilibrium value. Conversely, if Pc $\ll 1$, then diffusion occurs more rapidly than sintering, and it is likely that the concentration of H_2O will be in equilibrium during sintering.[12] If Pc ~ 1, then the diffusion and sintering occur over similar timescales, and the sintering is likely to occur among particles for which neither the initial nor the equilibrium H_2O concentration is valid, and for which evolving gradients of H_2O will occur. In this intermediate regime of Pc, a diffusion solution (e.g., Equations 7 with 9) along with Equation (10) is required to solve sintering problems.

Sintering involves the progressive decrease of porosity with time until a final equilibrium porosity is reached that is given by the percolation threshold. For monodisperse spherical glass beads, this is around $\phi = 0.03$, consistent with both experiments and theoretical determinations.[15,18,20,45–48] During this decrease in porosity, isolation of pores by pore pinch-off occurs; a process that begins as $t \to \lambda_b$. As λ_b is approached, not only does the porosity decrease substantially, but also the pore network permeability,[20,49] which becomes zero at the percolation threshold. Therefore, the end of sintering at $t = \lambda_b$ (or, equivalently, $\bar{t}_b = 1$) represents a transition

from an open-system that is permeable, to a chemically closed-system that is impermeable. In our dehydration sintering experiments, as diffusion occurs out of the glass beads, we assume that the boundary conditions are constant at $C = C_e$, where C_e is a constant low value consistent with low partial pressures of H_2O in dry furnace atmospheres. This assumption requires that the external furnace atmosphere and the pore network interior are connected and that there is no permeability limitation to the degree of "communication" between those two regions of the system. However, when the permeability drops to zero at λ_b, the transition to closed-system means that the H_2O that leaves the glass during the dehydration is not transported out of the pore network anymore, but essentially trapped. This H_2O remains in contact with the glass and so the partial pressure can equilibrate and effectively shut off diffusive mass transfer between the gas in the now-isolated bubbles and the glass surrounding them.

In the Pc $\gg 1$ regime, the process described above results in isolated bubbles in the sintered glass matrix that are predicted to be H_2O-poor because diffusion is inefficient compared with sintering in this scenario. Therefore, we anticipate that once the system becomes closed, diffusion of H_2O into the closed bubbles will continue at $t > \lambda_b$ for the time required for the partial pressure of H_2O to equilibrate in the bubble. Conversely, in the Pc $\ll 1$ regime, we anticipate that the isolation of bubbles will occur after diffusive equilibrium has been achieved, and so no further diffusive mass transport will occur when the system isolates. The Pc ~ 1 straddles these two regimes, and therefore we predict the result will be between these two end members. For Pc $\gg 1$, a central prediction is that pore isolation will occur before diffusion has completed. If the atmosphere surrounding the sintering material remains at low H_2O partial pressure, then this means that the effective distance that diffusion has to transport mass in order to equilibrate rises from R to L, where L is the sample lengthscale. The diffusion timescale therefore becomes $\lambda_d = L^2/D$, and because by definition $L > R$, we can see that the diffusion time becomes longer once the percolation threshold is crossed at $t = \lambda_b$. The magnitude of this increase in the diffusion time then depends on the ratio of L^2 to R^2. This interpretation is consistent with our data (Figures 4 and 5), which show that the mass loss slows down at the time $t = \lambda_b$ (Figure 5) compared with the diffusion solutions based on R as the controlled lengthscale.

The phenomenological observation from our experimental data is that the particle-scale diffusion of H_2O, captured by bulk sample mass loss, was interrupted before it could complete to equilibrium, shown by the change in the mass loss trend with time (Figure 4). Our analysis indicates that this "interruption" occurs at a time that is
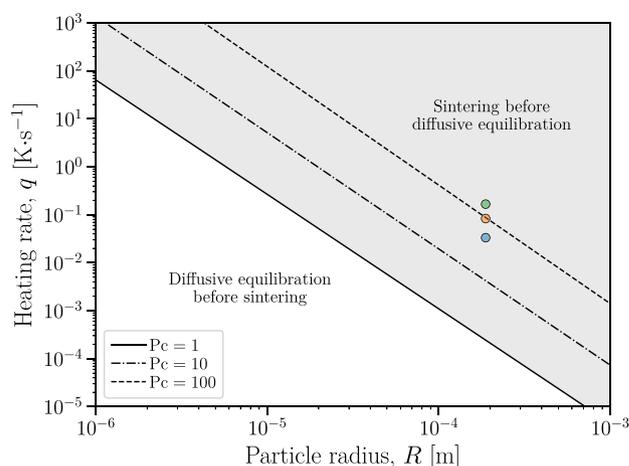
FIGURE 6 Regimes of mass loss during sintering for different initial values of particle size R (see text for details). The colored datapoints represent the experimental conditions used herein (blue, orange, and green: 2, 5, and 10 K min^{-1}, respectively; see Figures 4 and 5).

equal to the sintering timescale. Therefore, sintering completes before diffusion, and we could anticipate therefore that our experiments all occur in the Pc > 1 regime. However, it is also clear that some appreciable mass loss has occurred before sintering completes, and therefore the use of a singular pre-diffusion value of $\langle C \rangle$ is not appropriate for determining μ and the sintering rate. Based on these observations, it seems likely that our experiments occur in the intermediate regime between Pc $\gg 1$ and Pc $\ll 1$. For non-isothermal conditions, Equation (11) is not simple to evaluate because the "initial" background value of μ and D are transient and so, difficult to nominalize.

For our non-isothermal conditions, we can use Equations (4), (8), and (9) to assess numerically the value of heating rate q at which $\bar{t}_d = 1$ and $\bar{t}_b = 1$ occur at the same time. We term this heating rate the "critical rate" q_c, and if an experiment is performed at the critical rate, then that non-isothermal experiment will effectively be at Pc = 1. Similarly, if an experiment is performed at a rate greater than the critical rate, then the result will be Pc > 1. Procedurally, for this final scaling analysis, in order to solve for this coincidence of $\bar{t}_d = 1$ and $\bar{t}_b = 1$, we must implement the viscosity model from Wadsworth et al. (2014)[8] (Figure 1) rather than the viscosity model that depends on H_2O. This is because the H_2O-dependent model approaches un-physical viscosity values at the vanishing H_2O concentrations predicted as $\bar{t}_d \rightarrow 1$. Whereas, instead, the Wadsworth et al. (2014)[8] model, which is for nominally dry soda-lime-silica glass, is clearly a limiting case as H_2O approaches small values (Figure 1). Applying this approach, in Figure 6 we find q_c as a function of R for our glass properties (Figure 1), and for our initial and boundary conditions. As expected from our analysis of Pc

given above, the experiments performed here lie at $q > q_c$ and therefore Pc > 1. This shows that the other regime Pc < 1 could be accessed by using smaller particles or by conducting the sintering experiment at up to three orders of magnitude lower heating rates.

At supersaturations larger than those investigated herein and for which the diffusion distance $R \gg \sqrt{Dt}$ for any diffusion time t, diffusive mass loss from viscous particles may be superseded by nucleation of bubbles in the particle cores.[50] This is a situation in which complex effects can occur, including the clear competition between diffusive loss and bubble formation and growth.[50] When sintering is occurring simultaneously with this process, the expansion of particles driven by the growth of a free gas phase in bubbles can, presumably, alter the sintering kinetics. This is a situation that warrants future investigation.

6 | CONCLUSIONS

We have developed a theoretical framework for the diffusive mass transport during sintering. This is readily applicable to the end-member case where diffusion is rapid compared with sintering, such that spatial gradients of H_2O and physical properties do not develop on the timescale of pore network closure, and pore isolation occurs after diffusive equilibration. However, in the other end-member case, as well as for intermediate cases, we find that if diffusion is sluggish, then there is what might be termed a "diffusion crisis" at the percolation threshold, at which point the diffusion length scale of relevance jumps discontinuously from being the particle length scale to the sample or system length scale, inevitably slowing the diffusive mass transport. Here, we rely on volume average properties being relevant to the sintering dynamics. However, in systems of larger particles, it is possible that viscosity gradients that can arise from diffusion of H_2O could be sufficient to require a boundary layer approach, in which a certain surface-proximal volume is the "controlling volume" for sintering. Such larger systems warrant future investigation.

ORCID
Jérémie Vasseur https://orcid.org/0000-0002-0783-5065

REFERENCES
1. Prado MO, Zanotto ED, Fredericci C. Sintering polydispersed spherical glass particles. J Mater Res. 2003;18(06):1347–54.
2. Rahaman MN. Sintering of ceramics. CRC Press; 2007.
3. Chiang Y-M, Birnie DP, Kingery WD. Physical ceramics. NY: J. Wiley; 1997.
4. Scherer GW. Sintering of low-density glasses: I, theory. J Am Ceram Soc. 1977;60(5–6):236–9.
5. Scherer GW, Bachman DL. Sintering of low-density glasses: II, experimental study. J Am Ceram Soc. 1977;60(5-6):239–43.
6. Simchi A, Petzoldt F, Pohl H. On the development of direct metal laser sintering for rapid tooling. J Mater Process Technol. 2003;141(3):319–28.
7. Dillon R, Matheson L, Bradford E. Sintering of synthetic latex particles. J Colloid Sci.1951;6(2):108–17.
8. Wadsworth FB, Vasseur J, Von Aulock FW, Hess K-U, Scheu B, Lavallée Y, et al. Nonisothermal viscous sintering of volcanic ash. J Geophys Res Solid Earth. 2014;119(12):8792–804.
9. Vasseur J, Wadsworth FB, Lavallée Y, Hess KU, Dingwell DB. Volcanic sintering: timescales of viscous densification and strength recovery. Geophys Res Lett. 2013;40(21):5658–64. https://doi.org/10.1002/2013GL058105
10. Tuffen H, Dingwell DB, Pinkerton H. Repeated fracture and healing of silicic magma generate flow banding and earthquakes? Geology. 2003;31(12):1089–92. https://doi.org/10.1130/g19777.1
11. Wadsworth FB, Vasseur J, Schauroth J, Llewellin EW, Dobson KJ, Havard T, et al. A general model for welding of ash particles in volcanic systems validated using in situ x-ray tomography. Earth Planet Sci Lett. 2019;525:115726. https://doi.org/10.1016/j.epsl.2019.115726
12. Wadsworth FB, Vasseur J, Llewellin EW, Brown RJ, Tuffen H, Gardner JE, et al. A model for permeability evolution during volcanic welding. J Volcanol Geotherm Res. 2021;409:107118. https://doi.org/10.1016/j.jvolgeores.2020.107118
13. Wadsworth FB, Vasseur J, Llewellin EW, Dingwell DB. Hot sintering of melts, glasses and magmas. Rev Mineral Geochem. 2022;87(1):801–40. https://doi.org/10.2138/RMG.2022.87.17
14. Meurisse A, Beltzung JCJ, Kolbe M, Cowley A, Sperl M. Influence of mineral composition on sintering lunar regolith. J Aerosp Eng. 2017;30(4):04017014. https://doi.org/10.1061/(ASCE)AS.1943-5525.0000721
15. Wadsworth FB, Vasseur J, Llewellin EW, Schauroth J, Dobson KJ, Scheu B, et al. Sintering of viscous droplets under surface tension. Proc Math Phys Eng Sci. 2016;472(2188):20150780. https://doi.org/10.1098/rspa.2015.0780

16. Mackenzie JK, Shuttleworth R. A phenomenological theory of sintering. Proc Phys Soc B. 1949;62(12):833.

17. Frenkel J. Viscous flow of crystalline bodies under the action of surface tension. J Phys. 1945;9(5):385–91.

18. Wadsworth FB, Vasseur J, Llewellin EW, Dingwell DB. Sintering of polydisperse viscous droplets. Phys Rev E. 2017;95(3):033114. https://doi.org/10.1103/PhysRevE.95.033114

19. Kirchhof MJ, Schmid HJ, Peukert W. Three-dimensional simulation of viscous-flow agglomerate sintering. Phys Rev E. 2009;80(2):026319.

20. Wadsworth FB, Vasseur J, Llewellin EW, Dobson KJ, Colombier M, Von Aulock FW, et al. Topological inversions in coalescing granular media control fluid-flow regimes. Phys Rev E. 2017;96(3):033113. https://doi.org/10.1103/PhysRevE.96.033113

21. Okuma G, Kadowaki D, Hondo T, Tanaka S, Wakai F. Interface topology for distinguishing stages of sintering. Sci Rep. 2017;7(1):11106. https://doi.org/10.1038/s41598-017-11667-2

22. Sparks RSJ, Tait SR, Yanev Y. Dense welding caused by volatile resorption. J Geol Soc. 1999;156(2):217–25. https://doi.org/10.1144/gsjgs.156.2.0217

23. Wadsworth FB, Llewellin EW, Vasseur J, Gardner JE, Tuffen H. Explosive-effusive volcanic eruption transitions caused by sintering. Sci Adv. 2020;6(39):eaba7940. https://doi.org/10.1126/sciadv.aba7940

24. Bordia RK, Kang S-JL, Olevsky EA. Current understanding and future research directions at the onset of the next century of sintering science and technology. J Am Ceram Soc. 2017;100(6):2314–52. https://doi.org/10.1111/jace.14919

25. Hess K-UU, Dingwell DB. Viscosities of hydrous leucogranitic melts: a non-Arrhenian model. Am Mineral. 1996;81(9–10):1297–300.

26. Jewell JM, Spess MS, Shelby JE. Effect of water concentration on the properties of commercial soda-lime-silica glasses. J Am Ceram Soc. 1990;73(1):132–5.

27. Soares VO, Reis R, Zanotto ED, Pascual MJ, Duran A. Non-isothermal sinter-crystallization of jagged $Li_2O–Al_2O_3–SiO_2$ glass and simulation using a modified form of the Clusters model. J Non-Cryst Solids. 2012;358(23):3234.

28. Prado M, Dutra Zanotto E, Müller R. Model for sintering polydispersed glass particles. J Non-Cryst Solids. 2001;279(2):169–78.

29. Coumans JP, Llewellin EW, Wadsworth FB, Humphreys MCS, Mathias SA, Yelverton BM, et al. An experimentally validated numerical model for bubble growth in magma. J Volcanol Geotherm Res. 2020;402:107002. https://doi.org/10.1016/j.jvolgeores.2020.107002

30. Castro JM, Cordonnier B, Tuffen H, Tobin MJ, Puskar L, Martin MC, et al. The role of melt-fracture degassing in defusing explosive rhyolite eruptions at volcán Chaitén. Earth Planet Sci Lett. 2012;333–334:63–9. https://doi.org/10.1016/j.epsl.2012.04.024

31. Castro JM, Beck P, Tuffen H, Nichols ARL, Dingwell DB, Martin MC. Timescales of spherulite crystallization in obsidian inferred from water concentration profiles. Am Mineral. 2008;93(11–12):1816–22.

32. Crank J. The mathematics of diffusion. Clarendon Press; 1975.

33. Zhang Y, Ni H. Diffusion of H, C, and O components in silicate melts. Rev Mineral Geochem. 2010;72(1):171–225. https://doi.org/10.2138/rmg.2010.72.5

34. Zhang Y, Stolper EM, Wasserburg GJ. Diffusion of water in rhyolitic glasses. Geochim Cosmochim Acta. 1991;55(2):441–56. PMID: 11537201

35. Shelby J. A limited review of water diffusivity and solubility in glasses and melts. J Am Ceram Soc. 2008;91(3):703–8.

36. Mesko M, Shelby J. Water solubility and diffusion in alkali silicate melts. Phys Chem Glasses. 2001;42:173–8.

37. McGinnis P, Shelby J. Diffusion of water in float glass melts. J Non-Cryst Solids. 1994;177:381–8.

38. Gardner JE, Ketcham RA. Bubble nucleation in rhyolite and dacite melts: temperature dependence of surface tension. Contrib Mineral Petrol. 2011;162(5):929–43.

39. Wadsworth FB, Vasseur J, Casas AS, Delmelle P, Hess K-U, Ayris PM, et al. A model for the kinetics of high temperature reactions between polydisperse volcanic ash and SO2 gas. Am Mineral. 2021;106(8):1319–32. https://doi.org/10.2138/am-2021-7691

40. Mesko M, Shelby J. Solubility and diffusion of water in melts of a TV panel glass. Phys Chem Glasses. 2001;42(1):17–22.

41. Deubener J, Behrens H, Müller R, Zietka S, Reinsch S. Kinetic fragility of hydrous soda-lime-silica glasses. J Non-Cryst Solids. 2008;354(42):4713–8. https://doi.org/10.1016/j.jnoncrysol.2008.04.021

42. Ayris PM, Cimarelli C, Delmelle P, Wadsworth FB, Vasseur J, Suzuki YJ, et al. A novel apparatus for the simulation of eruptive gas-rock interactions. Bull Volcanol. 2015;77(12):1. https://doi.org/10.1007/s00445-015-0990-3

43. von Aulock FW, Kennedy B, Maksimenko A, Wadsworth FB, Lavallée Y. Outgassing from open and closed magma foams. Front Earth Sci. 2017;5. https://doi.org/10.3389/feart.2017.00046

44. Wadsworth FFB, Vasseur J, Llewellin EEW, Genareau K, Cimarelli C, Dingwell DB. Size limits for rounding of volcanic ash particles heated by lightning. J Geophys Res Solid Earth. 2017;122(3):1977–89. https://doi.org/10.1002/2016JB013864

45. Kertesz J. Percolation of holes between overlapping spheres: Monte Carlo calculation of the critical volume fraction. J Physique Lett. 1981;42(17):393–5.

46. Rintoul MD. Precise determination of the void percolation threshold for two distributions of overlapping spheres. Phys Rev E. 2000;62(1):68.

47. Elam WT, Kerstein AR, Rehr JJ. Critical properties of the void percolation problem for spheres. Phys Rev Lett. 1984;52(17):1516.

48. Vasseur J, Wadsworth FB. Sphere models for pore geometry and fluid permeability in heterogeneous magmas. Bull Volcanol. 2017;79(11):77. https://doi.org/10.1007/s00445-017-1165-1

49. Wadsworth FB, Vasseur J, Scheu B, Kendrick JE, Lavallée Y, Dingwell DB. Universal scaling of fluid permeability during volcanic welding and sediment diagenesis. Geology. 2016;44(3):219–22. https://doi.org/10.1130/G37559.1

50. Weaver J, Lavallée Y, Ashraf M, Kendrick JE, Lamur A, Schauroth J, et al. Vesiculation and densification of pyroclasts: a clast-size dependent competition between bubble growth and diffusive outgassing. J Volcanol Geotherm Res. 2022;428:107550. https://doi.org/10.1016/j.jvolgeores.2022.107550